Supporting Information: Charge-to-Spin Conversion by the Rashba-Edelstein Effect in 2D van der Waals Heterostructures up to Room Temperature

Talieh S. Ghiasi,[*,†,‡] Alexey A. Kaverzin,[†,‡] Patrick J. Blah,[†] and Bart J. van Wees[†]

†*Zernike Institute for Advanced Materials, University of Groningen, Groningen, 9747 AG, The Netherlands*

‡*Equal contribution*

E-mail: t.s.ghiasi@rug.nl

1. Sample fabrication and AFM characterization

Fabrication of the fully hBN-encapsulated van der Waals (vdW) heterostructure of TMD-graphene (Figure 1a) starts with separate exfoliation of the TMD, graphene and hBN on SiO_2/Si substrates. Optical contrast of the flakes with respect to the substrates, together with the height profiles, measured by Atomic Force Microscope (AFM), confirms that the selected flakes are monolayers. For fabrication of the vdW stacks we use a dry pick-up technique,[1] using poly(carbonate)(PC) and PDMS stamps. First, we transfer the monolayer (1L) graphene on the bulk hBN flake. In order to release the graphene flake, we melt the PC at 190 °C and we remove the PC in chloroform for 5 min. Further, the sample is annealed at 350 °C in Ar/H_2 atmosphere for 4 hrs. In the next step, we etch the graphene-bulk hBN stack into Hall-bar geometry by oxygen plasma, using a lithographically prepared PMMA mask (details of this technique will be explained in a separate publication).

Using another PC-PDMS stamp, we pick up the 1L hBN from the SiO_2/Si substrate that it is exfoliated on. The 1L hBN on PC-PDMS stamp is brought in contact with 1L TMD for pick up by using van der Waals forces. The 1L hBN/1L TMD stack on the PC-PDMS stamp is placed on top of the etched graphene-bulk hBN stack on SiO_2/Si substrate by micro-manipulators. The process of melting the PC and its removal in chloroform and further annealing in Ar/H_2 atmosphere is repeated, accordingly. The procedure for the full hBN-encapsulation of TMD-graphene heterostructure is followed by the fabrication of electrodes. The Ti/Au electrodes are made by using a pre-patterned (by EBL) PMMA mask. By E-beam evaporation of Ti/Au, we make the gold pads. The Co electrodes are fabricated by conventional EBL technique, using PMMA as the e-beam resist, followed by the deposition of Co at UHV atmosphere and lift-off in 40 °C acetone.

Figure 1b shows an AFM image (tapping mode) of the fully hBN-encapsulated 1L TMD-graphene on SiO_2/Si substrate. The height profile of each of the layers is shown in the inset, which confirms consistency with thicknesses associated with monolayers of TMD, graphene and hBN.[2,3] In the AFM image, we observe formation of bubbles at the interface between the

2D crystals. These bubbles that mainly originate from adsorbate molecules, indicate proper adhesion between layers of the vdW heterostructure, meaning that the area in between the bubbles is expected to be clean and adsorbate-free.

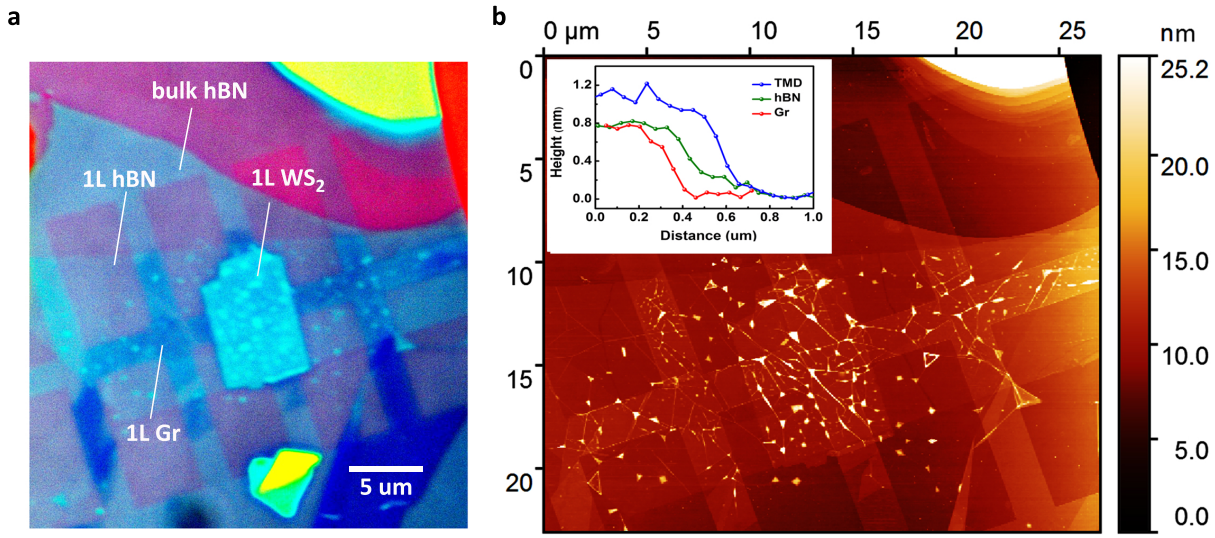

Figure 1: **Optical and atomic-force microscope (AFM) images** (a) Optical microscope image of the hBN-encapsulated WS_2-graphene heterostructure. (b) AFM image and height profile (inset) of the vdW stack (tapping mode). The thickness of the bottom hBN is about 14 nm.

2. Charge transport measurements

We perform four-terminal electrical measurements in order to characterize the charge transport properties of the TMD-graphene heterostructure. In Figure 2, we show the gate-dependence of the conductance measured through the TMD-covered graphene region. In order to measure the spin transport with magnetic field applied in and out-of-plane, discussed in this work, we had to bring the sample to ambient condition and change the sample rotator. In Figure 2, panel (a) shows the transport characteristics of the channel, for the measurements with an in-plane rotator (B applied in x-y plane) and panel (b) shows that of the out-of-plane rotator (B applied in x-z plane). We observe that the doping of the channel changes from p-doping to n-doping during the sample transfer.

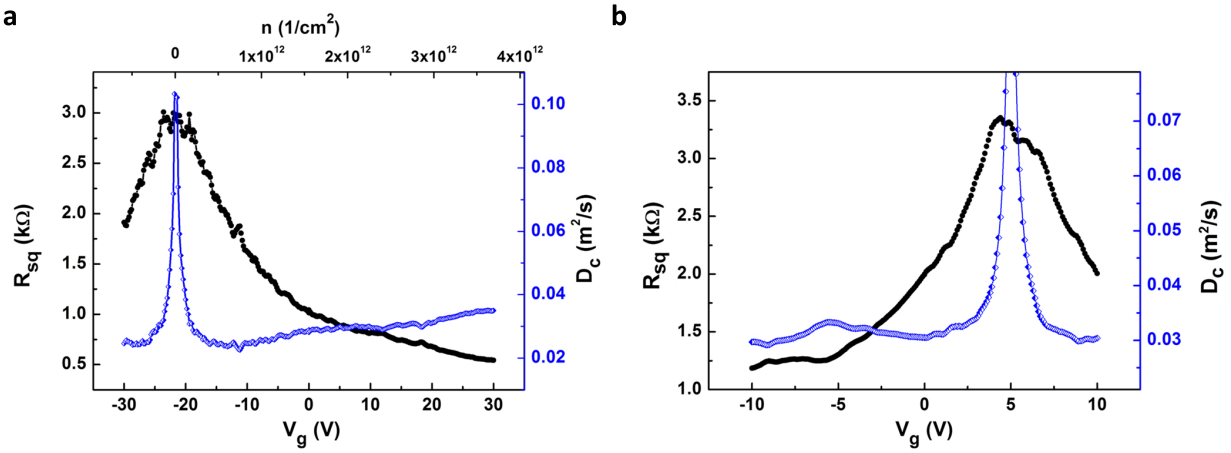

Figure 2: TMD-graphene charge transport characteristics. Square resistance (R_{sq}) and diffusion coefficient (D_c) of the WS_2-covered graphene channel versus gate-voltage (V_g) and density of charge carriers for Hanle precession measurements with B applied (a) in x-y plane (measured at 4.2 K) and (b) in x-z plane (measured at 10 K).

From the charge transport, considering the geometry of the channel, we extract the charge diffusion coefficient, used for our further analysis for spin transport (assuming $D_c = D_s$). The charge transport characteristics of the sample shows that the TMD-covered graphene region that is the focus of this work is electrically disconnected from the rest of the sample. Therefore, we restrict our measurements to the TMD-covered region as shown in Figure 1b of the manuscript.

The resistance of the contacts is estimated from a three-probe measurements with subtraction of channel resistance contribution (assuming homogenous channel). The resistances of the Ti/Au contacts are ~ 3 and 5 kΩ and those of the Co contacts are ~ 4 and 14 kΩ, measured at $V_g = 0\,V$ and $T = 4.2\,K$. The larger resistance of the contacts compared with that of the graphene channel suppresses the back-flow induced spin relaxation.[4]

3. Band structure of graphene in proximity of a monolayer TMD

In Figure 3 we show the typical band structure of graphene in proximity of a monolayer TMD, considering the K and K' valleys. In this heterostructure, the broken in-plane inversion symmetry creates out-of-plane spin-orbit field that changes sign from one valley to the other. However, breaking of the out-of-plane symmetry in the graphene because of the presence of the TMD leads to in-plane Rashba spin orbit fields that acquire directions perpendicular to the momentum of charge carriers. This gives a winding texture to the in-plane spins in the graphene Dirac cones in momentum space (Figure 3b). Direction of the spins in the two valleys can be resolved by considering preservation of time-reversal symmetry. Based on that, if momentum of an electron changes sign (from K to -K) the spin of the electron should also undergo sign reversal. This leads to opposite out-of-plane and in-plane spins in K and -K.

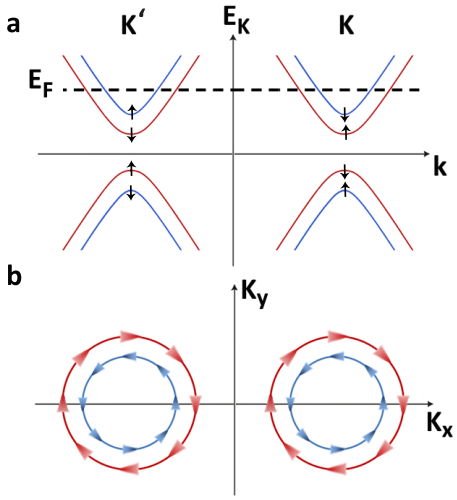

Figure 3: Spin texture in a typical band structure of graphene in proximity of a monolayer TMD. (a) Graphene Dirac cones in K and K' valleys. The black arrows show the out-of-plane spin polarization. The red and blue colors, corresponds to the opposite winding direction of the in-plane spins. (b) Fermi level contours in the momentum space.

In Figure 3 the black arrows represent the out-of-plane spin polarization in the spin-split bands and the red/blue arrows resemble the polarization direction of the in-plane spins where the color of each circle defines the overall winding direction. Therefore, the preservation of

the time-reversal symmetry and the sign reversal of the in-plane spin polarization lead to the same winding direction of the in-plane spin texture in the two valleys. This causes the same contribution of the two valleys in generation of non-equilibrium spin density by the charge current due to the Rashba-Edelstein effect.

4. Symmetrization and antisymmetrizations of Hanle precession measurements vs direction and magnitude of the in-plane magnetic field B

As discussed in the main manuscript, SHE and REE are expected to produce signals that obey specific symmetries with respect to the strength of magnetic field B and in-plane angle α under assumption that the ferromagnetic contact has opposite magnetization alignment for positive and negative B. The details on the magnetization alignment of contacts with respect to B are discussed in section 5. The symmetry table for the SHE and REE components is given in the main text. According to the table (anti-)symmetrizing the data with respect to B should already disentangle the REE and SHE contribution in the measured signal. However, we see from our analysis that the extracted symmetric vs B component of the data is neither symmetric nor anti-symmetric with respect to α whereas the SHE component should be purely anti-symmetric in α. This means that in our results we have an additional component that cannot be explained either by REE or SHE. Therefore, we perform further (anti-)symmetrization of our data with respect to α in order to extract purely REE and SHE associated components. REE is extracted by anti-symmetrizing the original data vs B and symmetrizing it vs α. SHE is extracted by symmetrizing vs B and anti-symmetrizing vs α. In the main manuscript we show in Figure 3 only the sum of the SHE and REE related contributions. The original full set of data is shown here in Figure 4 plotted for different angles α, after performing alignment of the Co contact magnetization at $\pm 3\,\mathrm{T}$ and sweeping the magnetic field from $\pm 0.6\,\mathrm{T}$ to $0\,\mathrm{T}$, respectively.

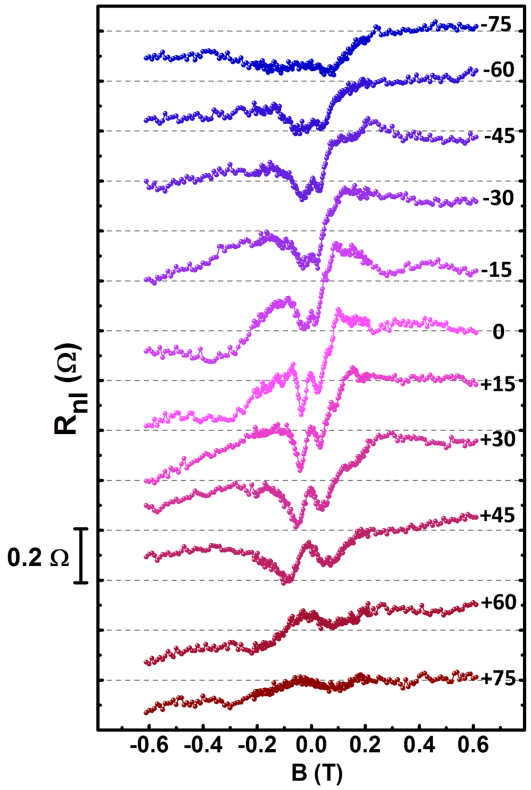

Figure 4: Nonlocal signal measured as a function of an in-plane magnetic field at different angles α from -75 to $+75$ degrees. Prior to the measurements in the positive/negative field range the Co contacts magnetizations are aligned by applying $+3\,\mathrm{T}/-3\,\mathrm{T}$.

In panels of Figure 5(a)-(i) we illustrate the decomposition procedure implemented here for the curve measured at $\alpha \approx -15$ deg. In panel (a) the measured data is shown. By anti-symmetrizing and symmetrizing it with respect to the magnetic field we obtain components shown in panels (b) and (c), respectively. Further, the obtained curves can be symmetrized and anti-symmetrized with respect to angle by using a corresponding curve measured at $\alpha \approx +15\,\mathrm{deg}$ (not shown in this figure). The resulting decomposition (panels (e), (f), (h) and (i)) gives a contribution coming from SHE (symmetric in B, anti-symmetric in α) and REE (anti-symmetric in B, symmetric in α) plus another two contributions (symmetric in B, symmetric in α (panel (i)) and anti-symmetric in B, anti-symmetric in α (panel (h)) the origin of which is not understood. The sum of SHE and REE components is plotted in panel (d) and gives the data that was shown in the main manuscript (Figure 3a) and was

used to compare with the model outcome. Note that the panel (g) shows the total unknown contribution that is still smaller in the magnitude compared to the REE component which is the main focus of this work.

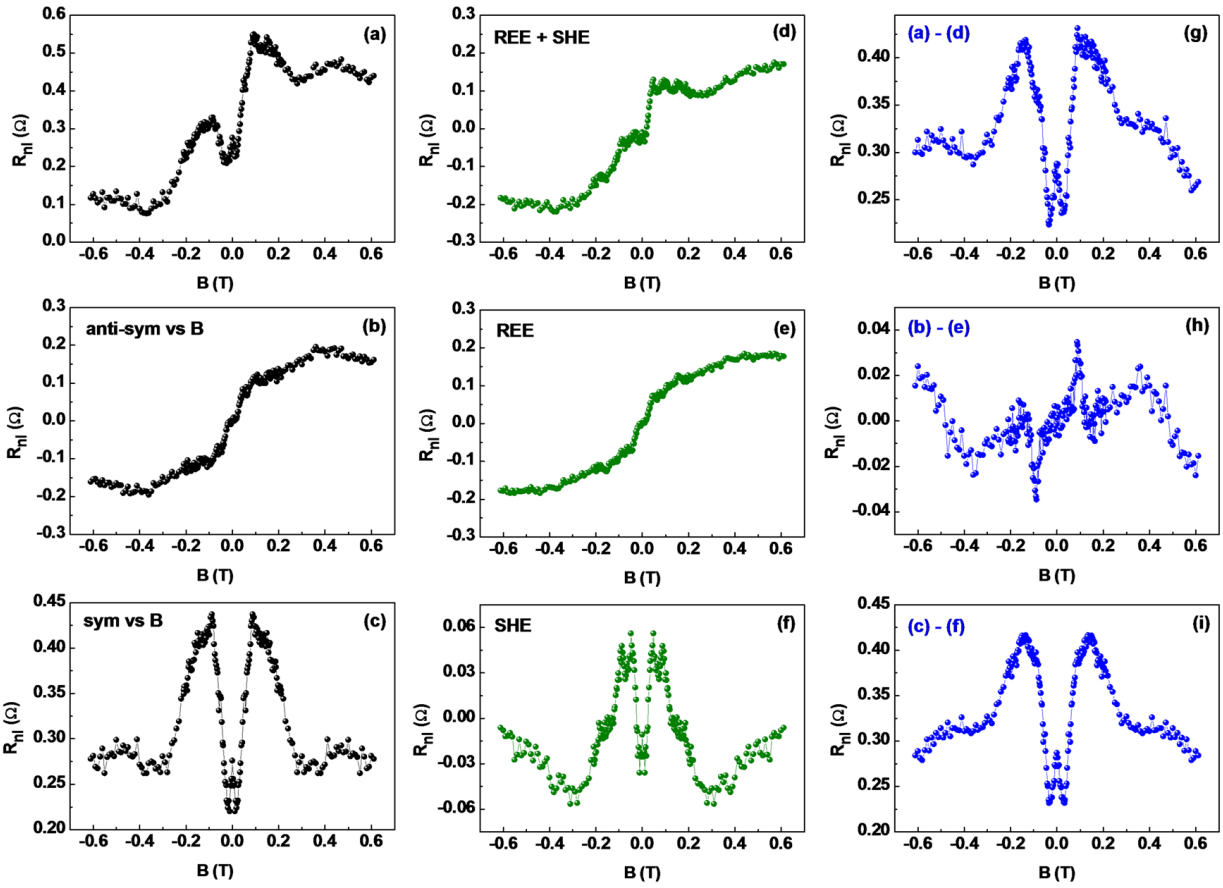

Figure 5: (a) Measured nonlocal resistance as a function of B for $\alpha \approx -15\,\text{deg}$. Panels (b) and (c) show the anti-symmetric and symmetric vs B components, respectively, such that (a)=(b)+(c). Panels (e) and (h) are symmetric and anti-symmetric vs α components, respectively, for the component (b) such that (b)=(e)+(h). Similarly (c)=(f)+(i). Panel (d) shows the signal that includes both SHE and REE and was fitted by the model, (d)=(e)+(f). Panel (g) gives the total unknown component that does not obey the expected symmetries, (g)=(h)+(i).

One of the possible explanations of the unknown component could be the generation of y-axis aligned spins due to misalignment of charge current in our sample. However, n_s^y produces the contribution to the measured signal that should also obey symmetries according to the symmetry table as we summarise here:

vs	n_s^x (REE)	n_s^z (SHE)	n_s^y
B	anti-sym	sym	anti-sym
α	sym	anti-sym	anti-sym

This means that presence of n_s^y should result in anti-symmetric vs B behaviour whereas we see the largest unknown contribution in a symmetric vs B component of the measured signal.

Another possible explanation is a non-homogeneous distribution of the magnetization over the ferromagnetic contact which can result in a signal that does not obey symmetry with respect to the angle α. Therefore, we assume the non-ideal behavior of Co contacts as the most probable explanation of the unknown contribution to our measurements.

5. Contact magnetization behaviour as a function of B

In Figure 6, we show the Hanle precession measurements performed with the in-plane magnetic field swept from $+0.6\,\mathrm{T}$ to $-0.6\,\mathrm{T}$ as the trace and from $-0.6\,\mathrm{T}$ to $+0.6\,\mathrm{T}$ as the retrace (B is applied under an angle of $\alpha \approx -15\,\mathrm{deg}$ in x-y plane). Before measuring the trace curve, a positive magnetic field of $+3\,\mathrm{T}$ is applied in order to align the contact magnetization. After crossing $B = 0\,\mathrm{T}$, the y-component of the magnetization of the contact switches to the opposite direction at $B \simeq -0.14\,\mathrm{T}$ which is seen as a jump in our signal indicated by the blue arrow. Similar behaviour is observed in the retrace with initial alignment of the contact magnetization at $-3\,\mathrm{T}$. The presence of these switches in the non-local resistance is another evidence of spin origin of our signals. Our detection circuit consists of two ferromagnetic electrodes which implies that in principle one should expect to see switches coming from both contacts whereas we observe only a single switch. Furthermore, our analysis (see Section 8) indicates that both contacts are spin sensitive and contribute to the spin transport detection with saturation fields along x axis being $B1_{sat} \simeq 0.09\,\mathrm{T}$ and $B2_{sat} \simeq 0.3\,\mathrm{T}$ where the value for $B1_{sat}$ is extracted as a fitting parameter of the model. As suggested by these saturation fields Co contacts have different magnetic shape anisotropies which is supported by the difference in their geometrical aspect ratios (contact widths are $W1 = 0.7\,\mu\mathrm{m}$ and $W2 = 0.5\,\mu\mathrm{m}$). Therefore, we attribute the absence of the second switch in our measured signal to a non-ideal behaviour of the contact magnetization with small magnetic shape anisotropy.

For a clear interpretation for our analysis we select the positive field range of the trace curve and the negative field range of the retrace curve implying that for the full B range in all the curves of both main manuscript and supplementary information (if not specified otherwise) the y component of the contact magnetization is aligned with y component of magnetic field.

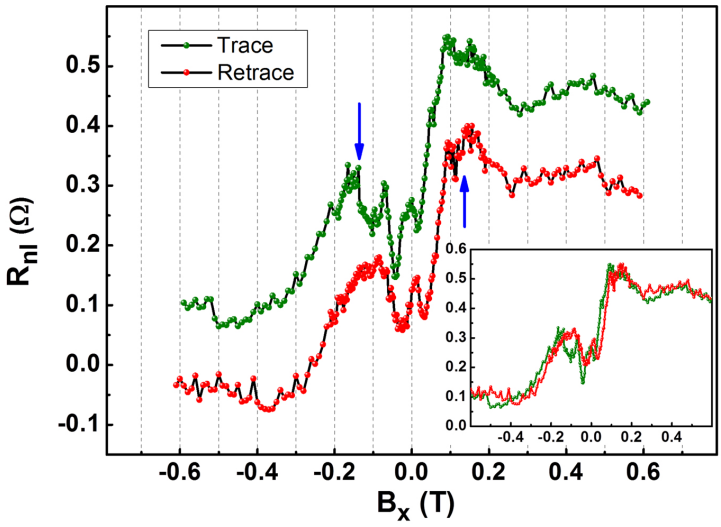

Figure 6: Trace and retrace of Hanle precession measurements with magnetic field applied in the x-y plane, under the angle of $\alpha \approx -15$ deg. The plots for the trace and retrace are shown with an offset in y axis with respect to each other for clear demonstration of the switch of contact magnetization. The blue arrows determine the switching point. The inset shows the trace and retrace without the offset.

6. Model description

In order to describe our results qualitatively and understand the interplay between various contributions we use finite element analysis (COMSOL) for modelling the coupled spin-charge transport in the TMD-graphene device. Both Rashba-Edelstein and spin Hall effects are introduced phenomenologically and are assumed to have an origin from the proximity of TMD. In addition to that the model includes the tilt of the contact magnetization direction with the applied external magnetic field in accordance with the Stoner-Wohlfarth model. For in-plane orientation of magnetic field the contact magnetization is assumed to have a single easy axis within the sample plane. For the out-of-plane direction of magnetic field the contact magnetization is assumed to have an easy plane (parallel to the sample plane) with an easy axis within that plane.

To model diffusive spin transport in our device we numerically solve a set of spatially two-dimensional drift-diffusion equations for three polarization directions of non-equilibrium spin densities n_s^x, n_s^y, n_s^z and electric potential V (n_s^i is expressed in electrical units of C/m^2).

The corresponding spin currents read as:

$$
\begin{aligned}
J_x^x &= -D\frac{\partial n_s^x}{\partial x};\\
J_y^x &= -D\frac{\partial n_s^x}{\partial y};\\
J_x^y &= -D\frac{\partial n_s^y}{\partial x};\\
J_y^y &= -D\frac{\partial n_s^y}{\partial y};\\
J_x^z &= -D\frac{\partial n_s^z}{\partial x} + SH\frac{\partial V}{\partial y};\\
J_y^z &= -D\frac{\partial n_s^z}{\partial y} - SH\frac{\partial V}{\partial x};\\
J_x^q &= -\sigma_0\frac{\partial V}{\partial x} + ISH\frac{\partial n_s^z}{\partial y} + IREn_s^y;\\
J_y^q &= -\sigma_0\frac{\partial V}{\partial y} - ISH\frac{\partial n_s^z}{\partial x} - IREn_s^x;
\end{aligned}
$$

where, for example, J_y^x is a current of spin aligned in x direction flowing in the y direction, J_x^q and J_y^q are x and y components of charge current. The diffusion coefficient D and conductivity σ of the system are connected through the Einstein relation $\sigma = De^2\nu$ with ν being density of states at the Fermi level. SH and RE are coefficients that determine the strength of induced spin Hall and Rashba-Edelstein effects. ISH and IRE are corresponding coefficients for inverse SHE and inverse REE and are chosen as $ISH = \frac{D}{\sigma}SH$ and $IRE = \frac{D}{\sigma}RE$ in order to obey reciprocity.

Using the continuity of the currents we formulate the diffusion equations for spin density and electric potential under an applied magnetic field $\overrightarrow{B} = (B_x; B_y; B_z)$:

$$
\begin{aligned}
-D\Delta n_s^x + \omega_z n_s^y - \omega_y n_s^z + \frac{n_s^x}{\tau_\parallel} &= RE\frac{\partial V}{\partial y};\\
-D\Delta n_s^y + \omega_x n_s^z - \omega_z n_s^x + \frac{n_s^y}{\tau_\parallel} &= -RE\frac{\partial V}{\partial x};\\
-D\Delta n_s^z + \omega_y n_s^x - \omega_x n_s^y + \frac{n_s^z}{\tau_\perp} &= 0;\\
-\sigma_0\Delta V &= -IRE(\frac{\partial n_s^y}{\partial x} - \frac{\partial n_s^x}{\partial y});
\end{aligned}
$$

where $\tau_\parallel$, $\tau_\perp$ are spin relaxation times for in and out-of-plane directions and spin precession is determined by $\omega_i = \frac{2\mu_B}{\hbar}B_i$.

It is important to note that SHE and REE are different in origin. REE creates a local spin density in the presence of the charge current while SHE creates a spin current which means that they enter the diffusion equations differently.

Gold contacts are incorporated into the model as regions with very high spin relaxation ($10000\tau_\parallel$) and large diffusion coefficient ($10000D$). To complete the problem the boundary conditions are defined as $V = 0\,\mathrm{V}$ and $n_s^x = n_s^y = n_s^z = 0\,\mathrm{C/m^2}$ at the boundary of the contact used for the ground and $\overrightarrow{J^q} = \overrightarrow{J}_{input}$ and $\overrightarrow{J^x} = \overrightarrow{J^y} = \overrightarrow{J^z} = \overrightarrow{0}$ A/m, where $\overrightarrow{J}_{input}$ is an input normal to the contact boundary charge current supplied at the source contact. At all other boundaries of the system the current normal to the boundary (both spin and

charge) is set to zero.

The geometry of the sample is copied from the optical (Figure 1c of the main text) and SEM images and implemented exactly into the geometry of the model. From the measured carrier concentration dependence of the device conductivity σ we extract the charge diffusion coefficient of the carriers D (see Section 2), both of which are directly incorporated as fixed model parameters. Initial values and acceptable limits of spin relaxation times for in-plane and out-of-plane polarizations are taken from the available literature[5,6] and later tuned in order to provide the best possible similarity to the complete set of the measured curves. Both ferromagnetic contacts are assumed to be spin sensitive and contribute to the measured spin signal.

The full set of equations is solved for each value of the applied magnetic field. Resulting maps of the spin density (Figure 2 of the manuscript) are then used to calculate an average spin density over the area underneath the Co contacts. The Stoner-Wohlfarth model is solved numerically for each field B/B_{sat} applied under an angle of $90\,\mathrm{deg}-\alpha$ with respect to the easy axis of the Co electrodes. We calculate the projection of the spin density on the contact magnetization direction that is picked up in the measurement and obtain a non-local signal as a function of the applied field.

7. REE and SHE coefficients

One can rewrite the REE spin current density source as $RE\frac{\partial V}{\partial y} = n_s^x/\tau_\parallel$, where n_s^x (or generalizing as n_s) is a uniformly generated spin density which is proportional to the charge current density $j_c = \sigma\frac{\partial V}{\partial y}$. It can be rewritten as $n_s = REj_c\rho\tau_\parallel$. In Ref.[7] the dimensionless REE efficiency α_{RE} is defined as the ratio between induced uniform spin density with respect to the supplied charge current density normalized by $2\upsilon_F$ (υ_F is Fermi velocity) which results in $\alpha_{RE} = 2\upsilon_F n_s/j_c = 2\upsilon_F RE\rho\tau_\parallel$. Under assumption for the value of contact polarizations $P1 = 0.3$ and $P2 = 0.2$ we extract the RE coefficient from our experimental data to be $400\,\mathrm{S/m}$ at $E_F \simeq 130\,\mathrm{meV}$ which results in $\alpha_{RE} \simeq 2.8$. This value exceeds the theoretically predicted value that is limited by 1. However, we note here that as emphasized in Ref.[7] α_{RE} is not a suitable figure of merit for Fermi energies far from the Dirac point which is the case for our estimation given above. Moreover, our model assumes an idealistic behavior of the Co contact and sample which can result in an overestimated value for the efficiency. In addition to that, presence of many fitting parameters (RE, $\tau_\parallel$, $\tau_\perp$) that are coupled to each other results in an uncertainty that can again explain the discrepancy between our estimations and theoretical calculations.

Note that the relation between the coefficient SH (defined here) and commonly used spin Hall angle θ_{SH} is $\theta_{SH} = SH/\sigma$. Here we extract $SH \simeq 0.13 \times 10^{-3}\,\mathrm{S}$ which results in $\theta_{SH} \simeq 0.13$ that is of similar order as reported in Ref.[8]

It is important to note here that in our particular case we are not able to extract the polarizations of the Co contacts independently from the strengths of REE and SHE effects. Therefore, the ratio of strengths of the two effect is the most reliable estimation that we can make as it does not depend on an average spin polarization of the contacts. For the extracted parameters we get $SH/RE = \frac{\theta_{SH}}{\alpha_{RE}} 2\upsilon_F\tau \simeq 0.33\,\mu\mathrm{m}$.

8. Fitting of the measured results

Fitting of the measured results is done with the help of the optimisation module from COMSOL. The measured REE component is mostly determined by the tilt of the contact magnetization in the sample plane meaning that the precessed spins (exploring the out-of-plane direction) give a minimal contribution to the measured signal due to relatively low relaxation time of the in-plane spins ($\tau_{\parallel}$ is in the order of few ps). In contrast the SHE contribution directly involves precession of spin from out-of-plane direction into in-plane direction and thus is sensitive to both spin relaxation times ($\tau_{\parallel}$ and $\tau_{\perp}$) and contact magnetization tilt. Therefore we use the SHE associated contribution of our data as an input for fitting procedure.

Furthermore, as discussed in section 4 there is an unknown contribution present in our measurements that does not obey expected symmetries. Non-ideal behaviour of the contacts can not only significantly influence the value of the saturation field (perpendicular to the contact geometrical easy axis) but can also cause a tilt of an easy axis by an arbitrary angle. In this case one can expect an additional component coming from both SHE and REE that is neither symmetric nor anti-symmetric with respect to angle $\alpha = 0\,\mathrm{deg}$ which results in an additional background after the data is anti-symmetrized with respect to $\alpha = 0\,\mathrm{deg}$. The larger the α, the larger this background can be. Therefore, we conclude that the most reliable data for fitting is the SHE component extracted from the measurements with smallest available angle difference that is $\alpha \approx \pm 15\,\mathrm{deg}$ (Figure 5f).

In Figure 7 we show the SHE contribution extracted from $\alpha \approx \pm 15\,\mathrm{deg}$ measurements together with the produced fit. The extracted fitting parameters are $\tau_{\parallel} = 3.5\,\mathrm{ps}$, $\tau_{\perp} = 90\,\mathrm{ps}$, contact polarizations $P1 = 0.3$ and $P2 = 0.2$, in-plane saturation field of the softer contact $B1_{sat} = 0.09\,\mathrm{T}$ (the saturation field of the harder contact $B2_{sat}$ is assumed to be $0.3\,\mathrm{T}$ which is estimated from the saturation level of the measurement taken at $\alpha = 0\,\mathrm{deg}$) and the background level $A = -0.02\,\Omega$. The margins for the given parameters are relatively large and therefore the extracted values should only be seen as estimations. In order to illustrate

the influence of each parameter on the final fit we deviate its value within a certain margin and calculate the deviating dependences which are shown in Figure 8.

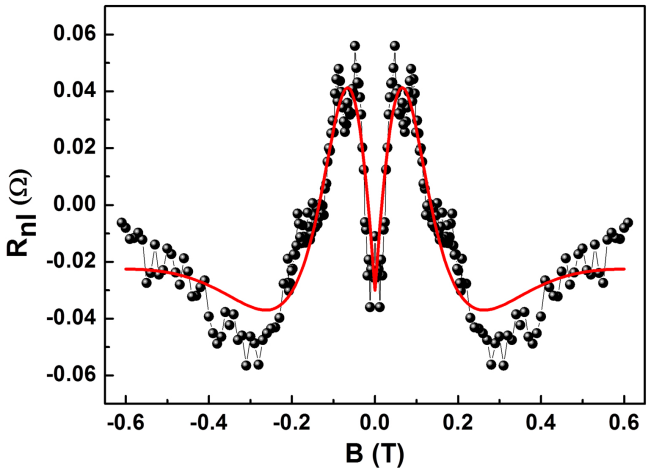

Figure 7: Nonlocal resistance as a function of B for $\alpha \approx -15\,\mathrm{deg}$ together with a fit from the model.

The extracted SHE component has a relatively small background that is likely to come as a result of (anti-)symmetrization procedures in the presence of an unknown component. In order to provide a better fit from the model we introduce a constant background $A = -0.02\,\Omega$.

It is apparent from Figure 8 that several parameters are heavily coupled with each other. To narrow down the range of possible parameters for the fitting procedure we used following restrictions that are based on the experience of our group and on the results published by other groups: $P1 \leq 0.4$, $P2 \leq 0.4$, $0.5\,\mathrm{ps} \leq \tau_{\|} \leq 5\,\mathrm{ps}$ and $5 \leq \tau_{\perp}/\tau_{\|} \leq 40$.

The size of the measured signal determines only the product of $RE * P$ (P is average polarization of Co contacts) and therefore we cannot independently determine them. For the final estimation of RE and SH coefficients we assume that $P1 \simeq 0.3$ and $P2 \simeq 0.2$. Furthermore, the ratio $P1/P2$ and parameters $\tau_{\perp}$ and $\tau_{\|}$ are also strongly coupled which means that one can obtain a satisfactory fit to the same data for the full range of $2\,\mathrm{ps} \leq \tau_{\|} \leq 5\,\mathrm{ps}$ (where $5\,\mathrm{ps}$ is the limit of the accepted range for the in-plane spin relaxation time) by

adjusting the other parameters accordingly.

Note that the in-plane saturation field for one of the contacts $B1_{sat}$ was found to be around 0.09 T which is not very typical, as the values obtained from different experiments[5] for similarly shaped contacts are in the range between 0.13 T and 0.3 T. However, it is apparent from Figure 8 that the position of the peak at $B \simeq$ 0.07 T is most sensitive to the value of $B1_{sat}$ which means that $B1_{sat}$ is very well defined by the fitting procedure and the value of, for example, 0.13 T would not give a satisfactory agreement with the measured data. This is in agreement with the presence of an unknown component associated with non-expected behavior of the contact magnetization.

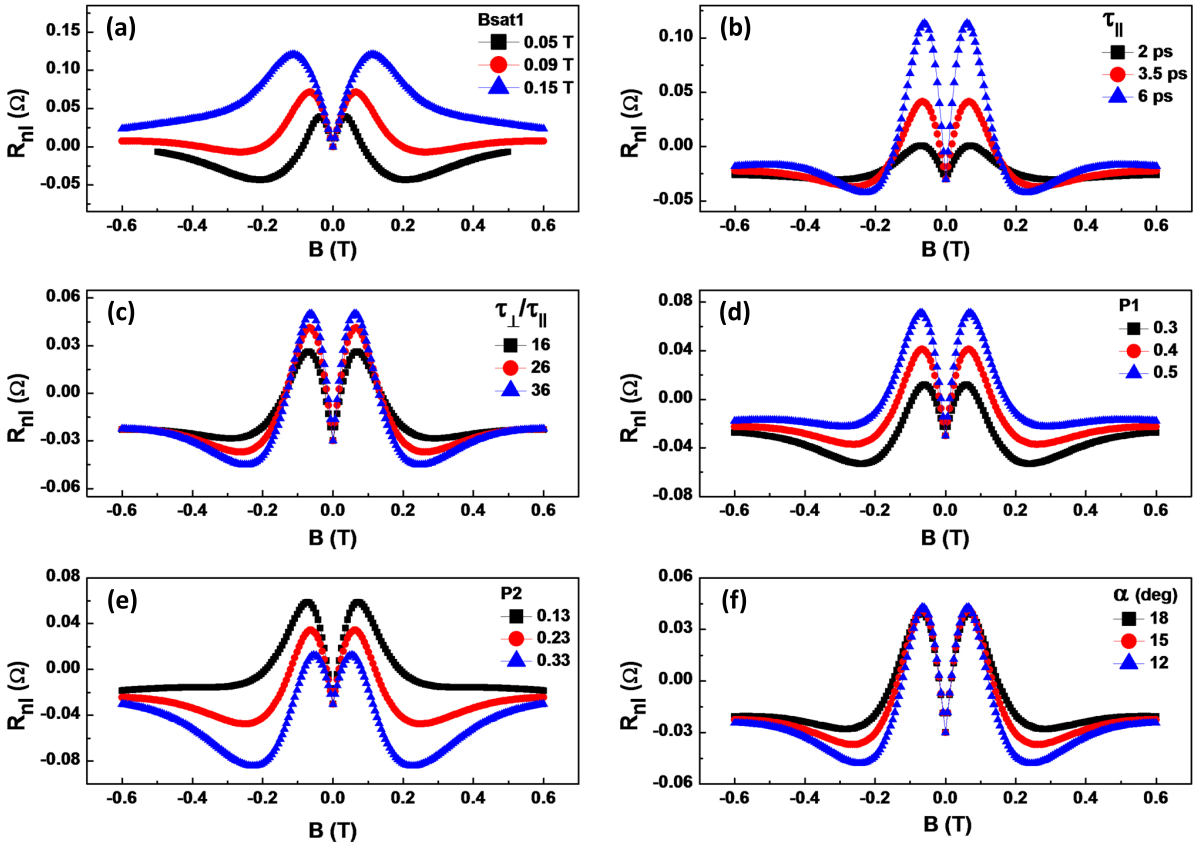

Figure 8: Panels (a)-(f) give the deviations of the fitting curve for each of the used fitting parameters. The red curve is the same in all the panels and gives the resulting fit shown in Fig. 7.

9. y-z plane Hanle precession measurements

By applying an out-of-plane magnetic field we can acquire additional information on the system parameters. In order to do that we reloaded the sample into a different setup where the out-of-plane rotation is accessible along the $y-z$ plane. We have measured the non-local signal as a function of magnetic field B applied along the direction oriented with angle φ with respect to the z axis. In Figure 9 we show the measured dependences at $\varphi = 0, \pm 45$ deg. Following the same logic as in section 10 we perform the anti-symmetrization procedure with respect to both B and ϕ and obtain a signal that here is much smaller in magnitude than any other signal measured in any other geometry. We associate this difference with the fact that the sample parameters changed significantly during the reloading procedure (mostly due to doping by water) which results in an undistinguishable from noise spin related signal.

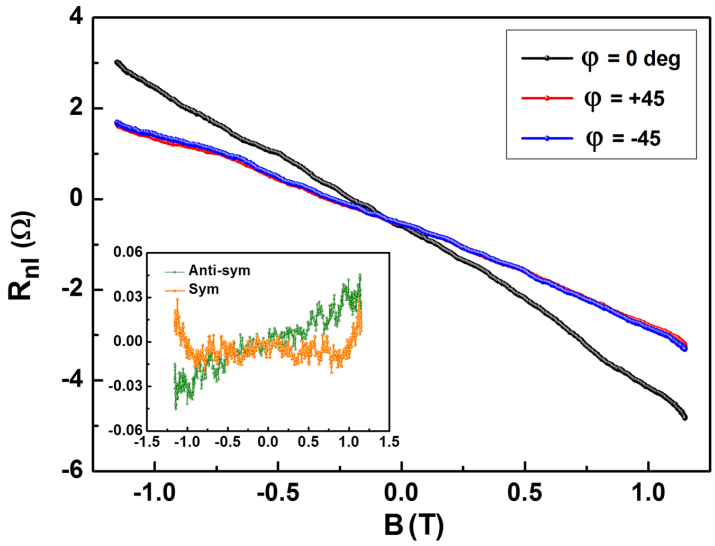

Figure 9: $y-z$ plane Hanle precession measurements. The inset is the symmetric and anti-symmetric components of the subtraction of the measurements performed at $\varphi = \pm 45$ degrees.

10. x-z plane Hanle precession measurements and modelling

In order to confirm the presence of both in-plane and out-of-plane spin polarization directions we reloaded our sample into another holder for the second time. In this holder magnetic field can be applied in any direction along the $x-z$ plane with θ being an angle between the magnetic field direction and z axis. The measurements were performed both at room temperature and 10 K. Room temperature measurements are shown in Figure 5 of the manuscript and 10 K measurements are presented here in Figure 10a. Having a B_z component of magnetic field one should expect additional components coming from Hall effect and magnetoresistance (MR). The non-local geometry of our measurements insures that charge current induced contributions are minimal which is confirmed by the low background level in all our measurements. However, due to the Ohmic spreading of the charge current there is a finite local current flowing between Co contacts along y axis which produces a measurable small Hall effect component. In order to exclude MR and Hall effect completely we again employ appropriate (anti-)symmetrization procedures. Firstly, to eliminate MR effect (or any other symmetric in B_z contributions) from our analysis we anti-symmetrize our measured dependences with respect to the applied B (main panel of Figure 10a). Further, SHE and Hall effect should give the same contributions for opposite angles $+\theta$ and $-\theta$ since the B_z component is the same. Therefore, anti-symmetrization of the data with respect to the angle θ should result in a component (shown in the inset) that can only be explained by REE. In the panel (b) we show the corresponding calculated contributions coming from REE for both angles 30 deg and 60 deg. The curves are calculated using the spin transport parameters extracted from the in-plane measurements. These curves qualitatively resemble similar behaviour as experimental data, however, the magnitude is different most likely due to the change in the sample parameters during the reloading procedure.

It is known that the in-plane saturation field of the contact magnetization direction is much smaller than that for the out-of-plane. Therefore, one should expect that with magnetic field applied at an angle θ in the $x-z$ plane the contact magnetization should

first mostly rotate within the $x-y$ plane until its tilting in this plane is saturated along x. After that the magnetization starts to tilt from the $x-y$ plane towards the z axis within the $x-z$ plane. Under this assumption the saturation point in the measured curves should be related to the ratio B_x/B_{sat} and scale accordingly with B_x if θ is changed (where B_{sat} is a saturation field within the $x-y$ along x direction). Our experimental observation of saturating behaviour as seen from Figure 10a (inset) is consistent with the described logic and is reproduced in the modelled dependences. Nevertheless, the behaviour beyond the saturation point is almost flat in the experimental data but is changing considerably in the calculated dependences. In order to explain these differences one should consider that the sample went through the procedure of unloading/loading from/into the setup which is known to significantly influence both the properties of the channel and of the contacts whereas we used the same spin transport parameters for modelling out-of-plane dependences as extracted from the in-plane measurements. Indeed, remeasured dependence of the channel resistance versus gate voltage (see Section 2) suggests a shift of the Fermi level in the sample from electron to hole-doped regime indicating major changes in the system properties presumably implying changes in all the relevant parameters including RE (which is observed to depend on the carrier density).

With an understanding of the origin of the saturation points in both measured and calculated data we can conclude that spin signal before the kink is mostly determined by the in-plane rotation of the contact magnetization and beyond the kink it is mostly determined by the precession of the spins out of the plane where it is picked up by the contacts with tilted out-of-plane magnetization. Therefore, by tuning appropriately the anisotropy level we can significantly flatten out the calculated dependences after the kink as it is shown in the inset of Figure 10b. This again points towards the change in the sample parameters after reloading it into the setup.

In conclusion, with out-of-plane applied field we also observe a component that can only be associated with REE, however, the exact behaviour and the magnitude of the measured

signal differs from the calculated dependences most likely due to the change in the sample parameters during the sample reloading procedure.

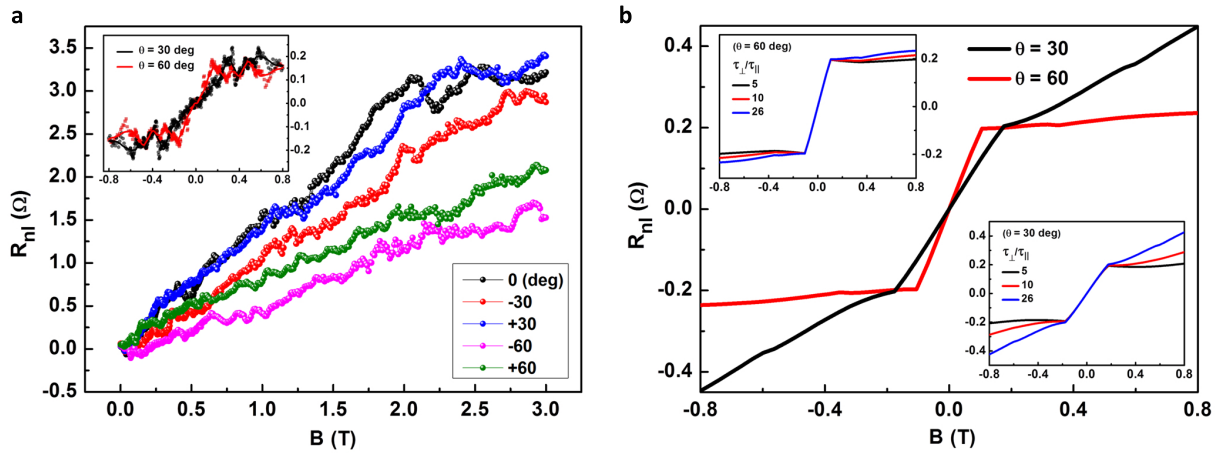

Figure 10: (a) Anti-symmetrized with respect to B non-local resistance measured for different directions of the applied field. Inset: measurements as in main panel but further anti-symmetrized with respect to θ. Measurements are performed at 10 K and with n $\sim -3.6 \times 10^{11}\,\mathrm{cm}^{-2}$. (b) Calculated non-local signal with spin transport parameters extracted from the in-plane measurements. Inset: same as in the main panel with having the anisotropy ratio $\tau_\perp/\tau_\parallel$ varied between 5, 10 and 26 for θ =30 and 60 degrees.

11. Possible contribution of the Hall effect of magnetic stray fields in the non-local voltage

Our measurements are performed in a non-local geometry in order to avoid contributions of a charge current in the region of the voltage probes. However, when the current source is applied on the arms of the graphene-cross (by the Ti-Au contacts), charge carriers can flow in and out of the graphene channel (along x-axis) due to current spreading and therefore the current along the y-axis would have a finite value that exponentially drops as a function of x (Figure 11). This charge current at the region of the ferromagnetic electrodes, can experience a Lorentz force of the stray fields generated by the magnetization of the Co electrodes. At zero magnetic field, when the magnetization of the electrodes is along their easy axis, the stray fields (along y-direction) do not affect the charge current distribution in that region. However, as soon as the magnetization of Co contacts acquires an x-component (by applying the external magnetic field along the x-axis), the z-component of the stray field can produce a transverse Hall voltage close to the edges of the Co electrodes which can result in a voltage between the two Co detectors. This out-of-plane stray field follows the behaviour of the Co magnetization and it increases up to a saturation level as soon as the magnetization direction gets fully aligned with the x-axis. Therefore the contribution of the stray field in the non-local voltage is anti-symmetric versus external magnetic field and so it follows the same symmetries as the REE spin signal as a function of magnetic field and the angle (α). Similarly, in the nonlocal measurements with out-of-plane external magnetic field, one can have the possible contribution from the stray field of the Co contacts when they develop a magnetization in the z-direction.

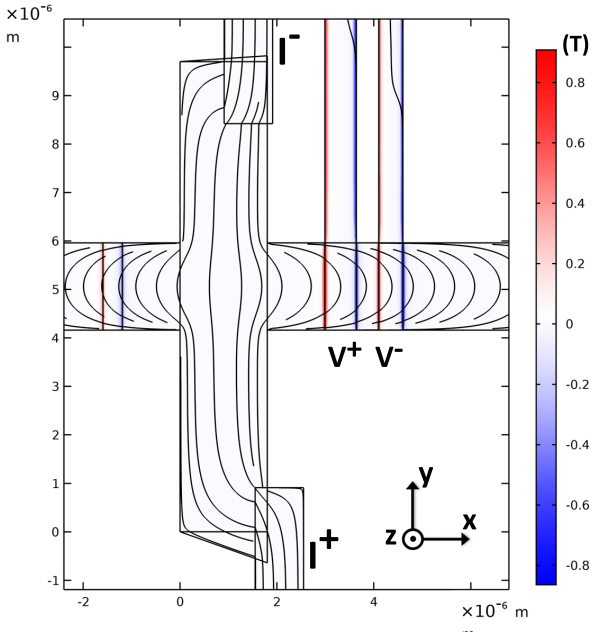

Figure 11: Current distribution (injected by the Ti-Au contacts) in the graphene Hall-bar that is modeled considering the exact geometry of the sample (resolved by SEM imaging). The external magnetic field is assumed to be applied along x-axis, large enough to fully saturate the magnetization of the Co voltage probes. Scale bar shows the magnitude of the z-component of the stray fields of the ferromagnetic electrodes, reaching a maximum at the edges of the Co strips.

Using finite element modeling (COMSOL), the change in the magnitude of the nonlocal resistance originating from the stray fields of the Co electrodes under an in-plane magnetic field is calculated as 77±35 mΩ. For this modeling we consider the exact geometry of our sample (resolved by SEM imaging) and we use the measured parameters (carrier density, resistivities) extracted from our device. The error bar is calculated considering the upper bound for inaccuracy of ±200 nm in determination of the position of the Co detectors or the width of the channel.

However, if we consider the measurements with the out-of-plane magnetic field (Figure 5 in the main manuscript), the magnitude of the regular Hall voltage (generated by the external magnetic field) resulting from the current flow in the y-direction in between the V+ and V- electrodes, is calculated to be about 46±12 Ω at B = 3 T. This is while, the result of the measurements (inset of Figure 5, main manuscript) shows the linear contribution of this

Hall effect, reaching the non-local resistance of $3.6\,\Omega$ which is about 10 times smaller than the calculated values. This discrepancy between the modeling and the measurement can be due to the presence of inhomogeneity in the sample that leads to a smaller current flow at the region of (or between) the Co probes. Therefore the actual contributions of the stray fields ($\sim 7.7 \pm 3.5\,\mathrm{m}\Omega$ for the in-plane measurement and $\sim 16 \pm 7.3$ mΩ in the out-of-plane measurement as subtraction of θ =+30 and -30 degree measurements) are expected to be 10 times smaller than the calculated values by the model. We assume that the inhomogeneity profile of the sample does not change significantly between the in-plane and out-of-plane measurement sets. As a result, the estimated contribution of Hall effect by the stray field is about one order of magnitude smaller than what we measure as REE spin signal and thus it is unlikely to explain our results.

As another proof for detection of the spin signal, we point out the fact that the measured non-local voltage in the inverse geometry is about 30% smaller compared to that of the direct geometry (inset of Figure 2d, main manuscript). This is while by the Onsager reciprocity, the magnitude of the signal in the direct and inverse geometries should be exactly the same. The deviation of the measured signal in the REE and IREE geometries can be attributed to the fact that the spin-injection efficiency by the ferromagnetic electrodes through hBN tunnel barrier is shown to be bias dependent[9] and therefore the spin polarization of the Co electrodes is different if they are used for the current injection (inverse geometry) compared with having them as voltage probes (direct geometry). This is in contrast with the detection of the Hall voltage (generated by the stay field) which should not be dependent on the spin polarization of the Co electrodes.

12. Gate-dependence of the non-local measurements

As shown in the main manuscript, the non-local measurements in the direct geometry are performed at different gate voltages. The anti-symmetric component of the R_{nl} versus B (associated to the REE) is shown in Figure 4a of the main manuscript. Here we show the symmetric component of the non-local resistance versus the in-plane B (Figure 12). As explained in section 4 of the SI, the symmetric component of the R_{nl} vs B at $\alpha \sim 0$ includes the contribution of the unknown component, exclusion of which is not possible from the data (requires anti-symmetriztion vs α). The gate-dependence of the symmetric component of the R_{nl} vs B (in Figure 12) can be because of the change in the efficiency of the SHE, the spin lifetime anisotropy and the overall spin transport properties of the channel and/or modulation of the unknown component. Quantification of the involved parameters requires further gate-dependence measurements (specifically for different α).

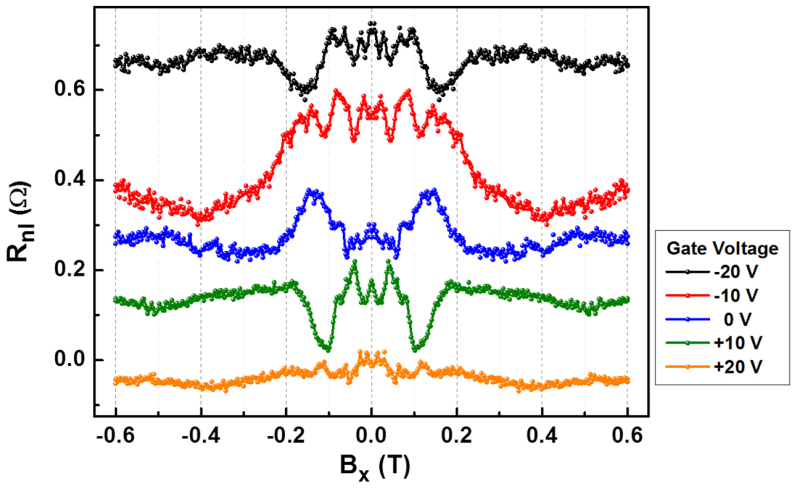

Figure 12: Symmetric component of the non-local resistance versus the in-plane magnetic field B_x. Measurements are performed at $\alpha \sim 0$ and T= 4.2 K.

13. Second harmonic measurements

Our measurements are performed by using a lock-in amplifier technique which allows to separate the linear and non-linear response of the system from each other. All our results presented elsewhere in this manuscript and supporting information are the linear response of the sample detected as the first harmonic signal. However, along with the first harmonic signal we also detected the second harmonic signal which is seen to give a clear Hanle-like dependence over the measured B range. In Figure. 13 we show the measured second harmonic signal at different gate voltages with magnetic field applied along x axis.

There are two possible reasons for the non-trivial second harmonic signal to appear in our system. First of all, a thermal gradient that originates from the Joule heating can result in a finite spin density due to spin Nernst and/or spin Seebeck effects. This means that a thermal gradient in the x direction can produce spin current in y direction with spin polarization in z direction (analogous to SHE in linear response) and spin density polarised in y direction (analogous to REE in linear response). Spin current in y direction results in a spin density of opposite polarization at opposite edges of the graphene channel and cannot be detected in our measurement geometry since the spin sensitive contact averages the spin potential over the full width of the channel. On the other hand, uniform spin density polarised along y axis can be detected and should result in a symmetric vs B Hanle curves. However, in this case we should be able to distinguish clearly the parallel and anti-parallel (with respect to the uniform induced spin density) states of the contact magnetization resulting in two P and AP signals of the same magnitude but opposite sign in a similar fashion as regular P and AP Hanle curves in only graphene samples. In our measurements we are not able to clearly identify the P and AP states and thus we cannot explain our results with the described above model.

An alternative explanation of the measured dependences is a non-linear detection of the spin density which is based on spin dependent conductivity in the presence of non-zero spin accumulation.[10] Following this mechanism the spin densities created in linear response of the

system can still be detected in the second harmonic with the difference that the detection is not sensitive to the sign of the spin density but only to its magnitude squared. This logic also results in a symmetric in B Hanle curves, however, at this stage we are not able to correlate the non-linear spin density detection with the measured dependences.

In conclusion, our measurements clearly suggest a presence of non-linear response of our sample which can either be associated with thermal gradient driven effects and/or non-linear spin detection mechanism. However, we are unable to clearly identify which of the two is responsible for the measured results strongly suggesting further measurements and analysis which will be presented in future publication.

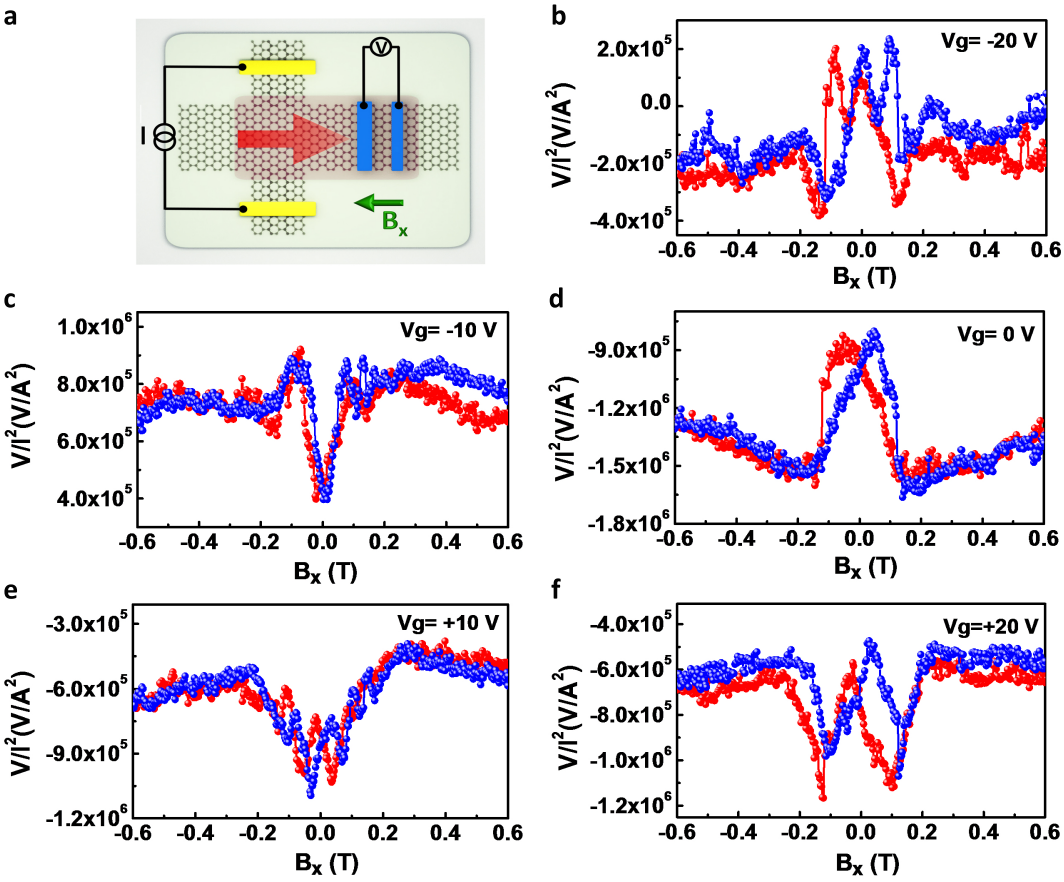

Figure 13: (a) Sketch of the device and the measurement geometry for the second harmonic measurements. The red arrow represents the thermal gradient ($-\nabla T$). (b)-(f) Modulation of the second harmonic signal (V/I^2) as a function of B_{x}, measured at different gate-voltages

References

(1) Zomer, P. J.; Guimarães, M. H. D.; Brant, J. C.; Tombros, N.; van Wees, B. J. Fast pick up technique for high quality heterostructures of bilayer graphene and hexagonal boron nitride. *Applied Physics Letters* **2014**, *105*, 013101.

(2) Ni, Z.; Wang, H.; Kasim, J.; Fan, H.; Yu, T.; Wu, Y.; Feng, Y.; Shen, Z. Graphene thickness determination using reflection and contrast spectroscopy. *Nano letters* **2007**, *7*, 2758–2763.

(3) Benameur, M.; Radisavljevic, B.; Héron, J.; Sahoo, S.; Berger, H.; Kis, A. Visibility of dichalcogenide nanolayers. *Nanotechnology* **2011**, *22*, 125706.

(4) Maassen, T.; Vera-Marun, I.; Guimarães, M.; Van Wees, B. Contact-induced spin relaxation in Hanle spin precession measurements. *Physical Review B* **2012**, *86*, 235408.

(5) Ghiasi, T. S.; Ingla-Aynés, J.; Kaverzin, A. A.; van Wees, B. J. Large proximity-induced spin lifetime anisotropy in transition-metal dichalcogenide/graphene heterostructures. *Nano letters* **2017**, *17*, 7528–7532.

(6) Benítez, L. A.; Sierra, J. F.; Torres, W. S.; Arrighi, A.; Bonell, F.; Costache, M. V.; Valenzuela, S. O. Strongly anisotropic spin relaxation in graphene–transition metal dichalcogenide heterostructures at room temperature. *Nature Physics* **2018**, *14*, 303.

(7) Offidani, M.; Milletarì, M.; Raimondi, R.; Ferreira, A. Optimal Charge-to-Spin Conversion in Graphene on Transition-Metal Dichalcogenides. *Physical review letters* **2017**, *119*, 196801.

(8) Safeer, C.; Ingla-Aynés, J.; Herling, F.; Garcia, J. H.; Vila, M.; Ontoso, N.; Calvo, M. R.; Roche, S.; Hueso, L. E.; Casanova, F. Room-Temperature Spin Hall Effect in Graphene/MoS2 van der Waals Heterostructures. *Nano letters* **2019**, *19*, 1074–1082.

(9) Gurram, M.; Omar, S.; van Wees, B. J. Bias induced up to 100% spin-injection and detection polarizations in ferromagnet/bilayer-hBN/graphene/hBN heterostructures. *Nature communications* **2017**, *8*, 248.

(10) Vera-Marun, I. J.; Ranjan, V.; Van Wees, B. J. Nonlinear detection of spin currents in graphene with non-magnetic electrodes. *Nature Physics* **2012**, *8*, 313.